Divalent Ion Selectivity in Capacitive Deionization with Vanadium Hexacyanoferrate: Experiments and Quantum-Chemical Computations

Kaustub Singh, Guanna Li, Juhan Lee, Han Zuilhof, Beata L. Mehdi, Rafael L. Zornitta, and Louis C. P. M. de Smet*

Selective removal of ions from water via capacitive deionization (CDI) is relevant for environmental and industrial applications like water purification, softening, and resource recovery. Prussian blue analogs (PBAs) are proposed as an electrode material for selectively removing cations from water, based on their size. So far, PBAs used in CDI are selective toward monovalent ions. Here, vanadium hexacyanoferrate (VHCF), a PBA, is introduced as a new electrode material in a hybrid CDI setup to selectively remove divalent cations from water. These electrodes prefer divalent Ca^{2+} over monovalent Na^+, with a separation factor, $\beta_{Ca/Na} \approx 3.5$. This finding contrasts with the observed monovalent ion selectivity by PBA electrodes. This opposite behavior is understood by density functional theory simulations. Furthermore, coating the VHCF electrodes with a conducting polymer (poly-pyrrole, doped with poly-styrenesulphonate) prevents the contamination of the treated water following the degradation of the electrode. This facile and modular coating method can be effortlessly extended to other PBA electrodes, limiting the extent of treated water contamination during repeated cycling. This study paves the way for tunable selectivity while extending the library of electrodes that can be successfully used in (selective) CDI.

1. Introduction

Capacitive deionization (CDI) is a water desalination technology in which two porous electrodes remove ions from water under the influence of an applied electric current or voltage.[1,2] Once removed, these ions are stored inside or at the surface of the capacitive electrodes. These electrodes can be fabricated out of the same materials with the same ion storage mechanism, like in conventional CDI, or from materials with different ion storage mechanism, as demonstrated in hybrid CDI (HCDI).[3,4] The choice of materials for electrode fabrication plays a crucial role in the performance of a CDI setup. Conventionally, carbon has been the material of choice for electrodes. The ions are removed from the water and stored in the micro/mesopores of the carbon.[5,6] Carbon has been the material of choice because of its low cost, easy availability, high conductivity, amphoteric behavior, and high surface area.[7,8] These attributes make it suitable for water desalination applications.[5,9,10] Carbon electrodes are, however, of limited utility for two reasons: First, they suffer from an unproductive reaction caused by the expulsion of ions with the same charge as that of the electrode, referred to as co-ion repulsion or ion swapping.[11,12] Second, they display an insufficient selectivity toward different ions.[13] Such selective removal of ions from water is, however, crucial

K. Singh, G. Li, H. Zuilhof, R. L. Zornitta, L. C. P. M. de Smet
Laboratory of Organic Chemistry
Wageningen University
Stippeneng 4, Wageningen 6708 WE, The Netherlands
E-mail: louis.desmet@wur.nl

K. Singh, L. C. P. M. de Smet
Wetsus
Oostergoweg 9, Leeuwarden 8911 MA, The Netherlands

G. Li
Biobased Chemistry and Technology
Wageningen University
Bornse Weilanden 9, Wageningen 6708 WG, The Netherlands

J. Lee, B. L. Mehdi
The Faraday Institution
Quad One
Harwell Science and Innovation Campus
Didcot OX110RA, UK

J. Lee, B. L. Mehdi
Department of Mechanical
Materials and Aerospace Engineering
University of Liverpool
Liverpool L69 3GH, UK

J. Lee
Helmholtz-Zentrum Dresden-Rossendorf
Bautzner Landstr. 400, 01328 Dresden, Germany

H. Zuilhof
School of Pharmaceutical Sciences and Technology
Tianjin University
Tianjin 300072, P. R. China

H. Zuilhof
Department of Chemical and Materials Engineering
King Abdulaziz University
Jeddah 21589, Saudi Arabia

**ADVANCED
SCIENCE NEWS**
www.advancedsciencenews.com

**ADVANCED
FUNCTIONAL
MATERIALS**
www.afm-journal.de

for industrial applications like resource recovery, production of fine chemicals, and water softening.[14]

A solution to a few of the above-mentioned issues of bare carbon is the use of ion-exchange membranes placed adjacent to it inside the desalination cell. This configuration is referred to as membrane capacitive deionization (MCDI).[15,16] The use of membranes in CDI cells has increased their ion removal and energy efficiency[17] and enabled versatile new cell architectures.[14] However, the high cost of the membranes poses a practicality issue. Another alternative to carbon lies with electrodes based on intercalation materials for CDI.[1,18,19] The crucial difference between intercalation materials and carbon is the storage mechanism of ions. Unlike storage on the pore surface as seen in carbon, ions in intercalation materials are inserted either into an interstitial lattice sites[20,21] or in between the layers of the material[22,23] under an applied electric current or voltage. This ion storage mechanism prevents the co-ion repulsion encountered in carbon-based electrodes, eradicating the necessity of membranes in high-efficiency CDI cells.[1] In addition, these materials retain the positive attributes of carbon, such as easy electrode preparation and improve upon the salt absorption capacity[24] and energy efficiency.[25,26] Furthermore, intercalation materials have also demonstrated inherent selectivity toward various ions,[14,27,28] unlike carbon which requires either membranes or surface modifications to gain high selectivity. The current study explores this inherent selectivity, exhibited by one of the Prussian blue analogs (PBAs), a class of intercalation materials.[29]

Prussian blue (PB), one of the oldest synthesized pigments, has the chemical formula $A_2M[Fe(CN)_6]$ in reduced form, where A is an alkali metal (Na, K). For PB, the element M is Fe, whereas for PBAs, M can be Ni,[30] Cu,[31] and V,[32] among other transition metal elements.[33,34] The use of PBAs in CDI is interesting because of their open crystal structure, customizable chemical composition, and inherent selectivity toward cations.[14,19,35] Furthermore, these electrodes have also been reported to be stable for up to 80 cycles under brackish water desalination conditions.[36,37] The ions removed from the water are stored in the interstitial lattice sites of the PBAs. This insertion is accompanied by a change in the oxidation state of a redox-active constituent of the PBA lattice.[38] Different cations intercalate into the lattice at different (reduction) potentials within the stability window of water.[14] This intercalation potential serves as a useful indication of whether the intercalation of a cation will be easy or difficult relative to another cation. Studies have shown that in a mixture of alkali metal ions, PB and its analogs demonstrate the strongest affinity toward Cs^+. This affinity reduces in the case of the alkali metals above Cs^+ in the group.[39,40] This trend of reducing the affinity of the PBA toward cations follows their insertion potential.[31,41] Taking advantage of this property, recent studies in CDI have also successfully demonstrated the use of PBA electrodes in the selective separation of monovalent over divalent ions.[19,35,42] However, systems for the selective removal of divalent ions based on PBA electrodes, important for applications such as water softening, surely require further development. Another area that requires improvement is the stability of PBA electrodes during repeated cycling.[43] It has been hypothesized that the electrodes dissolve due to the exchange of CN^- in the PBA lattice with OH^- from the aqueous solution.[21] This dissolution results in the release of undesired species into the treated solution, demanding an extra post-treatment step. To enable a wider utilization of PBA-based CDI technologies, this shortcoming must be addressed.

In this study, we introduce vanadium hexacyanoferrocyanate (VHCF) as electrode material in CDI, explain its ion selectivity by quantum chemical calculations, and develop a coating for the electrode to prevent treated water contamination. In brief, VHCF was synthesized, characterized, and used as an active electrode material for selective ion separation from a mixture of mono- and divalent ions, via HCDI. A schematic of the cell used for desalination is given in **Figure 1**. This cell configuration contains a cathode, made of VHCF particles embedded in a conducting carbon additive, a spacer channel for feed flow, and an oversized activated carbon anode,[44] isolated by an anion-exchange membrane (AEM) from the feed. The VHCF particles were characterized in detail using a variety of surface-sensitive, temperature-sensitive, and electrochemical methods. Selectivity experiments were performed on binary and ternary solutions of mono- and divalent cations. The stability of the VHCF electrodes was tested in single-salt solutions. Density functional theory (DFT) calculations on the crystal structures were performed within the VASP program[45] to elucidate the intercalation preference of the VHCF lattice toward different cations, and to compare it with that of nickel hexacyanoferrate (NiHCF), another widely used PBA in (selective) CDI.[1,14] Finally, the surface of VHCF electrodes was modified to prevent the release of ionic components of the electrode in the treated stream after electrode degradation. We show that this can be successfully achieved by coating the VHCF electrode with a protective layer of a conducting polymer polypyrrole-doped with poly(styrenesulfonate) (PPy/PSS), thereby reducing the direct contact of feed and the electrode. This study demonstrates the first-time use of a PPy/PSS layer to prevent contamination of treated water, for a divalent cation-selective PBA electrode, also shown in this study for the first time.

2. Experimental Section

2.1. VHCF Particles: Preparation and Characterization

The synthesis of VHCF-active particles was performed according to a modified coprecipitation adopted from literature.[32] A 40×10^{-3} M solution of VCl_3 (Alfa Aesar) was prepared in 200 mL of water containing 1% (v/v) HNO_3 (Sigma Aldrich). Simultaneously, a 20×10^{-3} M solution of $Na_4[Fe(CN)_6] \cdot 10H_2O$ (Sigma Aldrich) was prepared in 200 mL of water containing 1% (v/v) HCl (Sigma Aldrich). These acidified precursors were dropwise added to a 200 mL of 10% (v/v) HCl solution. The reactor was immersed in an oil bath, maintained at 70 °C, and the mixture inside was stirred at 600 RPM for ≈12 h. The precipitate formed was washed with a vacuum filtration unit, and the residue was dried overnight in a vacuum oven at 80 °C. The morphology of the VHCF particles was examined by a JEOL JSM 7001F field emission scanning electron microscope (SEM) at an acceleration voltage of 10–15 kV. The chemical composition of the VHCF particles was determined
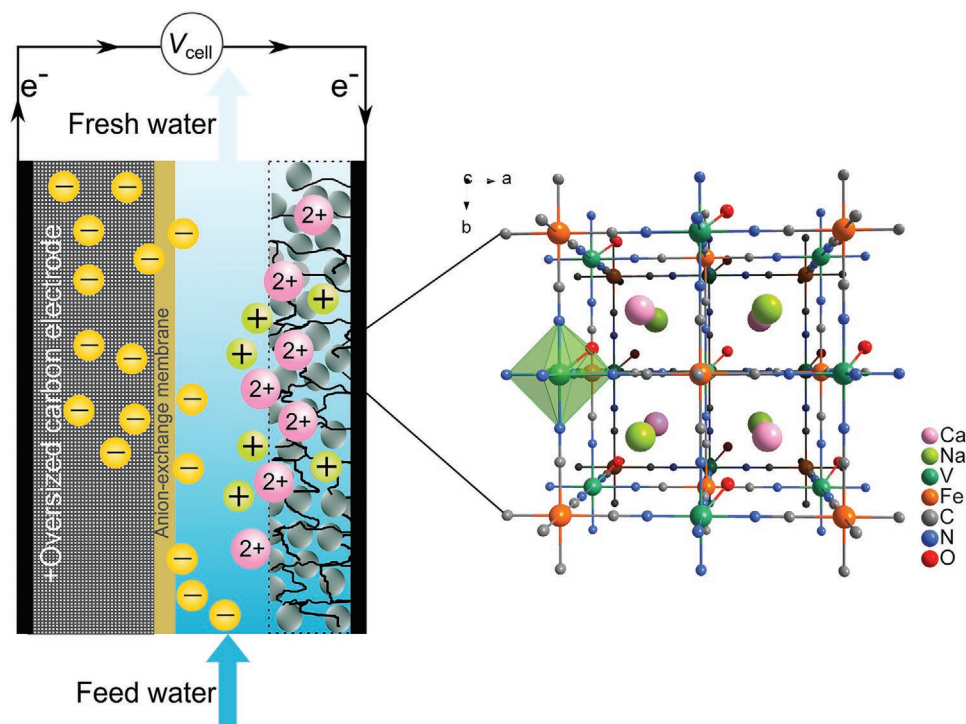
Figure 1. Schematic of a hybrid CDI cell with VHCF and an oversized carbon electrode, separated from the spacer by an anion-exchange membrane. A simplified version of the freestanding cathode shown here depicts its components as agglomerated VHCF particles (green spheres) interconnected by the conductive carbon additive (black irregular lines) to facilitate intraparticle electron transfer as well as that between the particles and the current collector. The schematic shows the moment of operation when cations (selectively) intercalate into the VHCF cathode and anions are adsorbed in the pores of the carbon anode, resulting in a desalinated feed at the outlet of the spacer channel. The inset depicts the unit cell structure of VHCF, modeled in the DFT calculations.

by energy-dispersive X-ray spectroscopy (EDS) with an INCA X-act EDS detector (Oxford Instruments). The spectra of ten spots on the different particles were measured using an accelerating voltage range of 15 kV and averaged. The crystallinity of the VHCF particles was assessed by powder X-ray diffraction (XRD), performed using a copper source for diffraction angles in the range of $10° < 2\theta < 70°$. Infrared (IR) spectroscopy was performed on the VHCF powder by a Bruker Tensor 27 spectrometer with platinum attenuated total reflection accessory. The X-ray photoelectron spectroscopy (XPS) spectrum of the VHCF particles was obtained by a JPS-9200 photoelectron spectrometer (JEOL, Japan) under ultrahigh vacuum, using a monochromatic Al Kα source at 12 kV and 20 mA and was processed by CASA XPS software (version 2.3.16) with Shirley background fitting correction. The water content in the VHCF powder was estimated by thermo-gravimetric analysis (TGA), performed under N_2 environment at the rate of 5 °C min^{-1} from 25 to 700 °C.

2.2. Electrode Fabrication

The dried VHCF powder was milled with the activated carbon (YP-80F) (Kuraray corp.) in a ball mill for 20 min. The resulting fine powder was mixed with poly(tetrafluoroethylene) (PTFE) (60% dispersion, Sigma Aldrich) in ethanol as a solvent and kneaded into a dough. The final composition of the dough added

was 8.5:1:0.5 for VHCF, AC, and PTFE, respectively. The partially dried dough was cold-rolled into 10 cm × 10 cm × 200 μm, freestanding sheets. The electrodes were dried at 120 °C overnight, under vacuum. Following the drying, the electrodes were stored in a desiccator.

2.3. PPy/PSS Layer Electrodeposition

The PPy/PSS layer was electrochemically deposited on the surface of the VHCF electrode to achieve a homogeneous layer. First, 150 mL of a solution containing 0.1 M PPy(Polymer, Sigma Aldrich) and 0.5 M PSS (sodium salt, Sigma Aldrich) was prepared. The VHCF freestanding electrodes were pressed and deposited on a graphite current collector in a rolling machine (MTI Corp) at room temperature. This VHCF-graphite composite electrode was then dipped in a PPy/PSS solution as a working electrode (WE). An oversized activated carbon was used as a counter electrode (CE) along with an Ag/AgCl electrode in 3 M KCl as the reference (RE). The PPy/PSS layer electrodeposition was carried out in a constant-current operation during which, a current of ≈150 mA g^{-1} was applied to the WE for 40 min. After the electrodeposition, the VHCF and the current collector became completely black. The rear of the current collector was carefully polished to remove any excess of physically bound PPy/PSS. The composite electrode was labeled as VHCF-PPy/PSS.

**ADVANCED
SCIENCE NEWS**
www.advancedsciencenews.com

**ADVANCED
FUNCTIONAL
MATERIALS**
www.afm-journal.de

2.4. Electrochemical Characterization and (Ion-Selective) Desalination

The electrochemical characterization of the electrodes was obtained from cyclic voltammetry (CV) experiments, carried out in a three-electrode cell with VHCF as WE, an activated carbon separated by an anion exchange membrane (AEM) as a CE, and an Ag/AgCl electrode as RE mounted close to the WE. The electrolytes were two different, 1 M solutions of NaCl and CaCl$_2$ each, with pH values of ≈2 and 7. In addition, a dilute HCl solution of pH = 2, containing no other cation, was also used as an electrolyte for CV. The electrode potential was varied from −0.2 to 1.05 V at the scan rate of 1 mV s^{-1} by a potentiostat (n.stat, IVIUM Technologies).

The selectivity experiments were performed in a hybrid CDI cell, as depicted in Figure 1, containing either the bare VHCF electrode or the PSS/PPy-coated VHCF electrode as cathode (0.1–0.2 g), and a YP-80F carbon electrode (10 cm × 10 cm × 500 µm, 0.6–0.8 g) as anode, separated by a porous spacer channel of thickness 500 µm. The weights of the cathode and anode were matched according to the adsorption capacities reported for PBAs (35–45 mg g^{-1})[18,26,46] and AC (10–15 mg g^{-1}).[47,48] An AEM was used to isolate the anode from the spacer channel, in order to prevent the influence of the carbon electrode on VHCF electrodes. Feed solutions with different kinds and concentrations of cations were treated by the cell to investigate the affinity of VHCF electrodes. The compositions of these feeds, namely, F1, F2, F3, and F4, and their corresponding pH are given in **Table 1**. The pH of the MilliQ water used to prepare the solutions was ≈6.5.

A batch of 50 mL of ion mixture was desalinated under a recycle condition by the VHCF hybrid cell. The ion removal was performed first under a constant-voltage operation. For absorption, a cell voltage of −1 V was applied for 0.5 h. The sample was taken after 0.5 h from the diluate reservoir to measure the ion concentration via ion chromatography (Eco IC, Metrohm). The VHCF electrode was regenerated by applying a cell voltage of +1 V for 0.5 h in a regeneration electrolyte containing the same cations as the ones in the diluate used during absorption. The end of these operations completed one full cycle. The chambers were flushed with MilliQ water in between the adsorption and desorption steps to prevent contamination of the diluate. Seven cycles were performed to continuously reduce the concentration in the diluate.

To understand how the VHCF electrodes performed upon continuous cycling, a hybrid cell containing a VHCF cathode and a carbon anode was cycled continuously in 20 × 10^{-3} M

single-salt solutions of NaCl and CaCl$_2$, respectively. The reservoir volume was 5 L. The cell was run for 40 cycles in a constant-voltage mode with steps of 0.5 h of operation, each at 1 and −1 V and the conductivity was recorded at the outlet. The electrodes were analyzed via post-mortem XRD.

2.5. Quantum Chemistry

All spin-polarized DFT calculations were performed using the Vienna Ab initio Simulation Package (VASP, version 5.4).[45,49] The Perdew–Burke–Ernzerhof (PBE) functional based on the generalized gradient approximation (GGA) was chosen to account for the exchange-correlation energy.[50] A plane-wave basis set in combination with the projected augmented wave (PAW) method was used to describe the valence electrons and the valence-core interactions, respectively.[51] The kinetic energy cut-off of the plane wave basis set was set to 400 eV. Gaussian smearing of the population of partial occupancies with a width of 0.05 eV was used during iterative diagonalization of the Kohn-Sham Hamiltonian. The threshold for energy convergence for each iteration was set to 10^{-5} eV. Geometries were assumed to be converged when forces on each atom were less than 0.05 eV Å^{-1}. Both atomic positions and lattice constants were fully optimized during the bulk calculation. The calculated lattice constants were 10.20 Å for the cubic NiHCF ($a = b = c$; $\alpha = \beta = \gamma = 90°$) and 7.24 Å for the rhombohedral VHCF ($a = b = c$; $\alpha = \beta = \gamma \neq 90°$) (detailed structural information available as .cif). The Brillouin zone integration and k-point sampling were done with a Monkhorst–Pack scheme of a 4 × 4 × 4 and 2 × 4 × 4 grid points for the unit cells and the 2 × 1 × 1 supercells of NiHCF and VHCF, respectively.[52,53] The DFT+U method was applied to deal with the on-site self-interaction error among the d electrons, and the U_{eff} values of Fe, Ni, and V were set as 1, 3, and 3 eV, respectively. The Van der Waals (vdW) interactions were included by using Grimme's DFT-D3(BJ) method, as implemented in VASP.[54] The calculations were done with intercalated cations with no hydration shell and with cations with six water molecules around them to understand the effect of solvent on the selectivity.[55]

3. Results and Discussion

3.1. VHCF Powder Characterization

The proposed synthesis route was chosen so that the vanadium precursor remains as V(IV) during the reaction with the [Fe^{2+}(CN)$_6$]$^{[4-]}$ group in the acidified reaction mixture. The addition of HNO$_3$ in the vanadium precursor solution results in the oxidation of V(III) to V(IV), which is characterized by a final blue color of the precursor solution, as depicted in Figure S1 (Supporting Information). The addition of V(IV) and [Fe^{2+}(CN)$_6$]$^{[4-]}$ precursors into an acidified aqueous reaction mixture, instead of adding one reactant to the other, kept the molar ratio of the reactants constant in the reaction mixture during the addition process. The acidification of the reaction mixture has been shown to retard

Table 1. Concentration of cations and the pH of the feed solutions treated by a hybrid CDI cell to investigate the affinity of VHCF electrodes toward different ions.

Feed	Li$^+$ (mM)	Na$^+$ (mM)	Ca^{2+} (mM)	Mg^{2+} (mM)	pH
F1	–	10	10	–	6.1–6.2
F2	–	10	–	10	6.6–6.8
F3	–	10	10	10	7.3–7.4
F4	10	–	10	–	6.7–6.8

the rate of coprecipitation between the precursors.[30,32] The delayed formation of the first crystals during the reaction, after the dropwise addition, gave an indication of the retarded rate of coprecipitation, which helps in formation of lattices with higher crystallinity.[32] The acidified reaction mixture coupled with the easy availability of V(IV) results in a facile growth of VHCF particles. SEM images of the synthesized VHCF particles are given in **Figure 2a**,b and Figure S2 (Supporting Information), showing an agglomera-

tion of particles, as seen for other PBAs such as NiHCF.[26] The size of these agglomerates range between 0.5 and 5 µm. Figure 2b shows the particles at 22 000× magnification, revealing that the agglomerates of ≈500 nm diameter have a flake-like morphology.

The XRD pattern of the VHCF powder was compared to that of the NiHCF powder to highlight the analogous nature of the two PBAs. The VHCF synthesis resulted in a well-defined and crystalline lattice, as seen in the XRD pattern of the VHCF
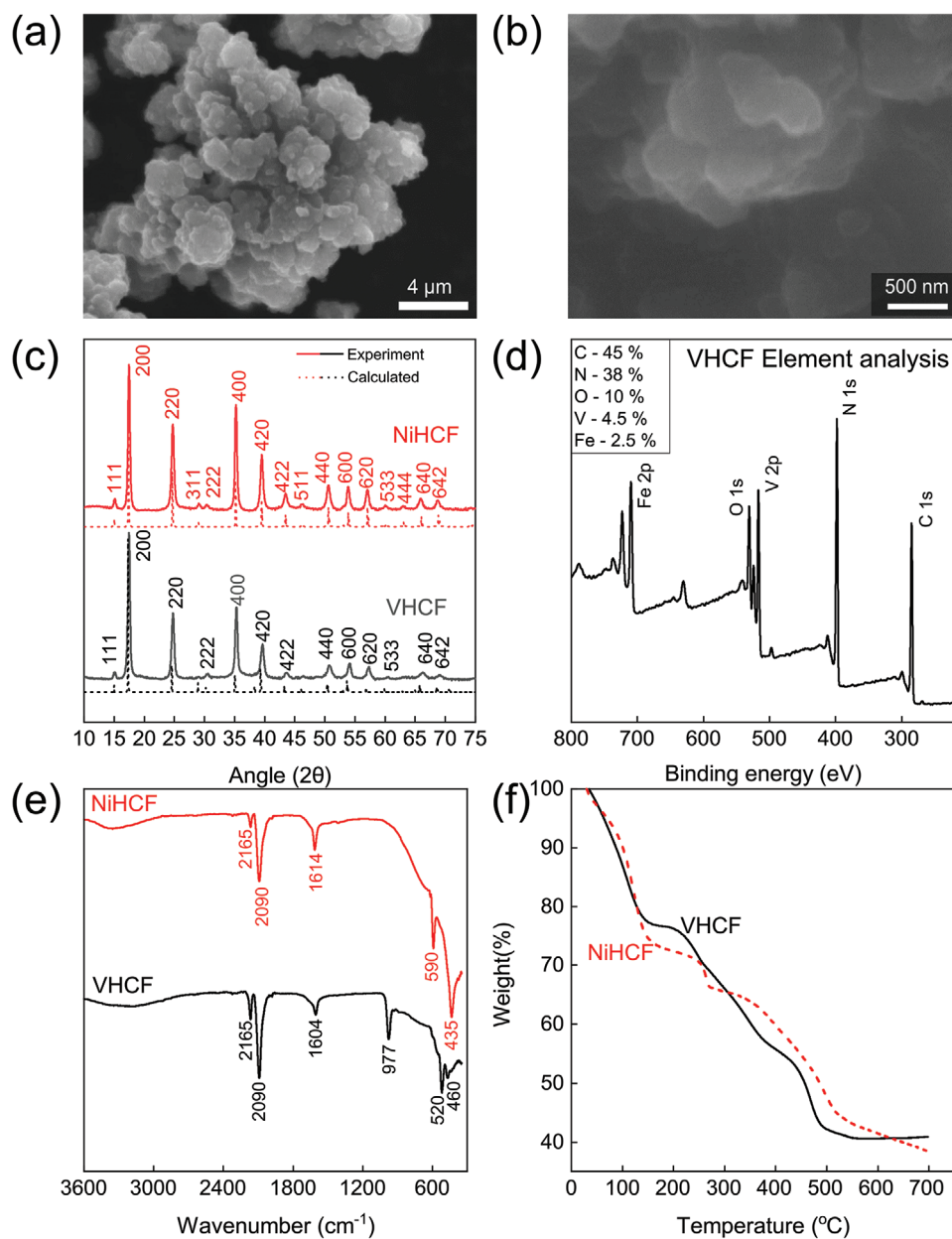

Figure 2. Characterization of the VHCF powder synthesized via a bulk coprecipitation reaction. Data for NiHCF, prepared via a similar coprecipitation method detailed elsewhere,[26] are also provided along with VHCF for comparison. a,b) SEM images of VHCF powder obtained at 4500× and 22 000× magnifications. c) Measured (solid lines) XRD patterns of as-prepared VHCF (black) powder and NiHCF (red) powder and the predicted (dashed lines) XRD peaks from the $DFT_{crystal}$ models with labeled characteristic planes. d) A wide XPS spectrum indicating the elements and their ratios in the VHCF powder. e) IR spectra of the VHCF (black) powder compared with that of NiHCF (red) powder with labeled characteristic stretching. f) TGA spectra of the VHCF (black) powder compared with that of the NiHCF (red) powder.

powder in Figure 2c. A comparison of VHCF diffractogram (black) to that of NiHCF (red) confirms that the VHCF structure is that of a PBA. The peaks in the NiHCF diffractogram are characteristic of a cubic lattice,[30,56] while the structure of VHCF can be ascertained to fit either a cubic or rhombohedral lattice, considering the high degree of overlap between them. The exact structure of VHCF may vary between these two lattice types, as is usually seen for PBAs.[57] Nevertheless, the XRD patterns presented in Figure 2c agree well with the diffractograms reported elsewhere for an electrochemically-deposited VHCF thin film,[58] and with the patterns predicted by the DFT calculations for the model crystals of both NiHCF and VHCF. The agreement between the experimental and the calculated diffraction pattern of VHCF is especially remarkable as it confirms our placement of O atom, present in the V=O bond, in the lattice toward the interstitial site, as illustrated in Figure 1. Interestingly, the peak positions appear to be shifted to higher angles for VHCF when compared to NiHCF. A closer look at the reflections of (200), (400), and (420) planes of VHCF and NiHCF particles, as shown in Figure S3 (Supporting Information), confirms this observation. This results in a d_{100} lattice spacing, calculated using the (h00) peaks shown in Figure 2c, of 10.15 Å for VHCF, compared to 10.2 Å for NiHCF. This value is within the range of values reported in the literature for VHCF (10.1 Å[59] and 10.19 Å[60]).

An XPS wide scan, presented in Figure 2d, confirmed the presence of iron, vanadium, carbon, and nitrogen in the VHCF lattice. As expected, the most abundant elements in the powder were carbon and nitrogen, followed by oxygen, vanadium, and iron. The presence of vanadium at a peak position of 516.6 eV in the XPS spectrum implies the presence of V(IV).[58] The presence of oxygen in the structure may come from water molecules residing either in the interstitial sites in the center of the lattice, as confirmed by the TGA measurement of the VHCF powder (Figure 2f), or bound to the transition metal.[61] The presence of vanadium as vanadyl, VO^{2+}, in the lattice also contributes to the total oxygen content. The V/Fe ratio of 1.7 indicates a presence of the higher number of $Fe(CN)_6$ vacancies in the lattices or the presence of interstitial vanadyl ions, as hypothesized earlier in a work that reported a V/Fe ratio of 1.5 for a thin film electrode.[58]

A similar trend in the elemental content of the VHCF powder was obtained by EDS measurements (Figure S2, Supporting Information). Carbon and nitrogen were the most abundant elements, the V/Fe ratio was 1.61, comparable to the ratio obtained from XPS, indicating the similar elemental composition in the bulk and on the surface of the particles, and sodium, only detected by EDS, was the least-abundant element. The amount of iron was one-sixth of both carbon and nitrogen, which can be attributed to the $Fe(CN)_6$ moieties in the lattice. A Fourier transform infrared (FTIR) spectrum, presented in Figure 2e, highlights the molecular vibrations in the VHCF lattice. The transmission peaks around 2090, 2165, and 440–520 cm^{-1} correspond to the characteristic stretching vibration of $-Fe(II)-C\equiv N-$, $-Fe(III)-C\equiv N-$, and $-M-C-$ bonds, respectively, as reported elsewhere.[61–64] These peaks also prove the presence of both Fe(II) and Fe(III) in the as-prepared VHCF particles, as reported earlier.[65] This feature of

the VHCF particles is also seen in narrow XPS scan of Fe, as shown in Figure S4. The V=O stretching was observed at 978 cm^{-1}, in line with literature for vanadyl ions.[32,59] The broad peak around 3300 cm^{-1} and the sharp peak around 1600 cm^{-1} can be attributed to the zeolitic and coordinated water present in the VHCF lattice, respectively.[32] The FTIR spectrum of the prepared VHCF powder is comparable to that of the NiHCF, with the only exception of $-M-C$ stretching, confirming the analogous nature of VHCF and NiHCF PBAs. Finally, the result of the thermogravimetric analysis (TGA) of the VHCF powder is provided and compared with that of NiHCF powder in Figure 2f. Weight loss was observed in three regimes. The first regime starts from 100 °C, indicating a weight loss of 22% related to the loss of structural water, as indicated by the IR transmission peaks and the presence of extra oxygen in the XPS analysis of the VHCF powder. This is lower than the amount seen in NiHCF (≈30%). The second and third regimes are associated with the evolution of HCN (180–280 °C) and decomposition of the electrode (>300 °C), similar to the reports in literature.[65]

3.2. Electrochemical Characterization of Electrodes

The VHCF electrodes were electrochemically characterized by CV. Such characterization is crucial as it provides insight into the redox activity of the electrode, associated here with cation intercalation, and it indicates the affinity of the electrode toward different ions.[28]

The voltammograms of VHCF electrodes, carried out in single-salt solutions of NaCl and $CaCl_2$ at two different pH of 2 and 7, are shown in **Figure 3a**,b. The voltammogram of $MgCl_2$ at pH = 2 is given in Figure S5 (Supporting Information). For a neutral feed solution with pH = 7, the VHCF electrodes exhibited a higher capacity in $CaCl_2$ in comparison to NaCl, evident from the area enclosed by the respective voltammograms in panel (a) (25.4 ± 0.3 C g_{VHCF}^{-1} in NaCl vs 42.8 C g_{VHCF}^{-1} in $CaCl_2$ solution). Interestingly, at pH = 2 the areas enclosed by the voltammograms of NaCl and $CaCl_2$, as shown in panel (b), increase to 38.2 ± 1.3 and 52.2 ± 1.7 C g_{VHCF}^{-1}, respectively. Interestingly, the reduction in pH increased the redox activity of the VHCF electrode resulting in more pronounced and distinct oxidation and reduction peaks related to (de)intercalation of Na$^+$ and Ca^{2+} in the lattice. This is, to the best of our knowledge, the first proof of the intercalation of any divalent ion in VHCF lattice at neutral and low pH. It also demonstrates a reliable operation of the electrodes at low pH, commonly encountered during recycling of metals in real-life applications. Furthermore, the voltammograms shown in Figure 3b give the first indication toward the relative preference of VHCF electrode toward divalent Ca^{2+} at $E_{red} \approx 0.55$ V, against monovalent Na$^+$ ions, with $E_{red} \approx 0.4$ V versus Ag/AgCl. A higher intercalation potential for the divalent ions indicates easier intercalation: after the deintercalation process, the ions with more positive reaction potential will be intercalated first. This voltammogram hints at the higher affinity of the VHCF electrodes toward divalent ions. The redox peaks which appear at
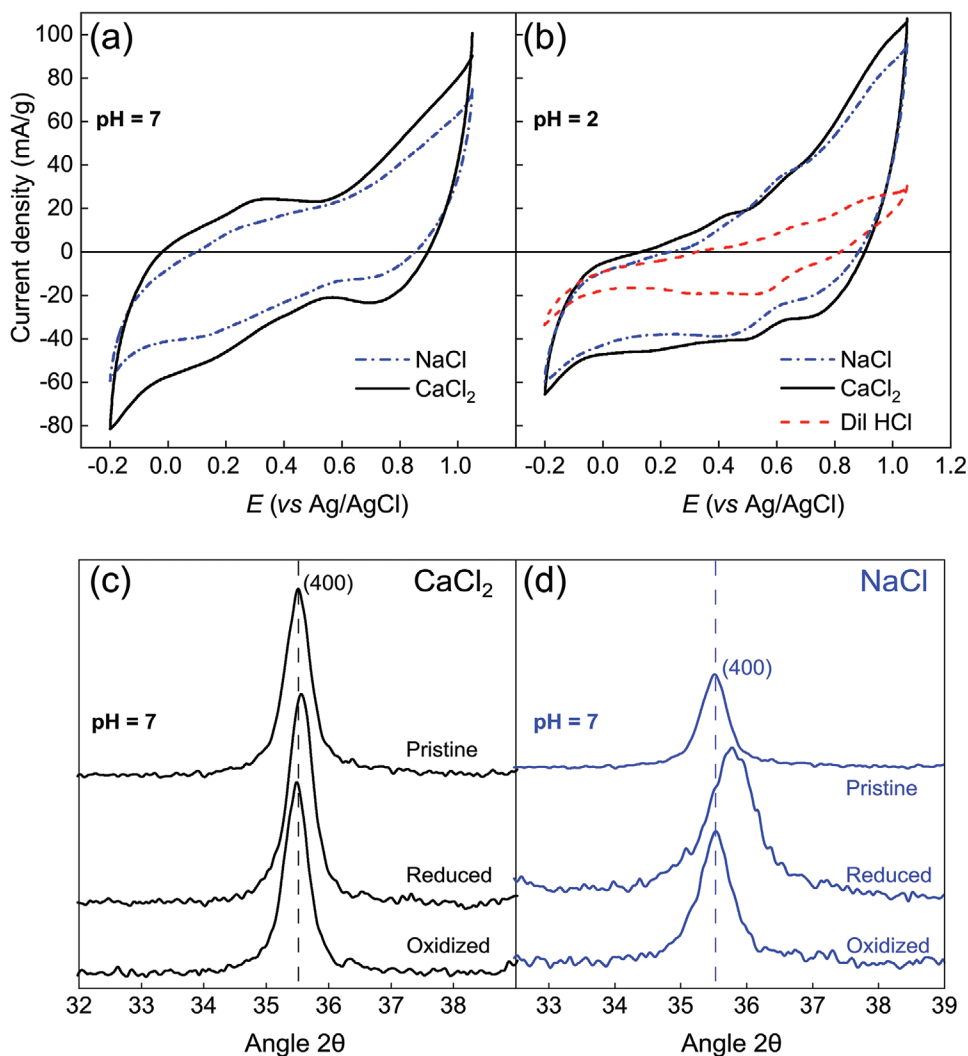
Figure 3. Electrochemical characterization of VHCF electrodes in a three-electrode cell by cyclic voltammetry in single-salt solutions of NaCl and CaCl$_2$ at a) pH = 7 and b) pH = 2, obtained at a scan rate of 1 mV s^{-1}. The voltammogram obtained in diluted HCl solution (pH = 2) is given by the red curve in panel. b) The post-mortem XRD patterns comparing the (400) plane peak of the VHCF lattice in pristine electrode with the oxidized, and reduced electrodes cycled in c) CaCl$_2$ and d) NaCl solution under neutral pH conditions.

pH = 2 cannot be due to extra H$^+$ (de)intercalation, as they remain absent from the voltammogram obtained in a dilute HCl solution that contains neither Na$^+$ nor Ca^{2+}. This implies that in the salt-containing solutions, Na$^+$ and Ca^{2+} remain the prominent adsorbing ions. The voltammograms presented in Figure 3a,b for NaCl differ from those previously reported in the literature for VHCF; for instance, the peak positions and the number of oxidation and reduction peaks.[32,58,59] These differences can be attributed to either the type of electrode: thin film (order of 10 nm—seen in literature[58]) versus sheet electrodes (200–300 μm—used in this study) or the CV conditions—acidic electrolytes (acid concentration > 3 M in literature) versus neutral to mild acidic (pH = 2–7 electrolyte used here). Since, as mentioned earlier, this is the first time that divalent cations have been inserted into the lattice of VHCF, no such comparison can be made with literature for Ca ions.

Other than the CV peaks, the proof of insertion of both mono- and divalent cations into the lattice is provided by the post-mortem XRD of VHCF electrodes cycled in CaCl$_2$ and NaCl, as shown in Figure 3c,d, respectively. A closer look at the diffraction pattern of Ca^{2+} indicates a positive shift in the position of the (400) peak during intercalation (reduction of Fe^{3+} to Fe^{2+}) of Ca^{2+} from 35.53° for the pristine electrodes to 35.58° for the reduced electrodes, indicating a contraction of the lattice. The exact direction of contraction and expansion will depend on the lattice symmetry. During deintercalation (oxidization of Fe^{2+} to Fe^{3+}) of Ca^{2+}, the (400) peak shifts rather clearly to a lower angle of 35.48°, indicating an expansion of the lattice. A total change of 0.1° was obtained between VHCF electrodes, fully intercalated and deintercalated in CaCl$_2$ electrolyte. Remarkably, a similar contraction and expansion of the lattice during (de)intercalation, as presented here for VHCF electrodes, has been reported for Na$^+$ in NiHCF electrodes with a comparable difference in lattice spacing between the oxidized and the reduced electrode.[56] Similarly, for intercalation and loss of Na$^+$, the (400) peaks show a strong positive shift from

**ADVANCED
SCIENCE NEWS**

www.advancedsciencenews.com

**ADVANCED
FUNCTIONAL
MATERIALS**

www.afm-journal.de

35.53° to 35.78° following the intercalation (reduction of Fe^{3+} to Fe^{2+}) of Na^+ into the lattice and deintercalation of Na^+ (oxidization of Fe^{2+} to Fe^{3+}) brings the (400) peak back to the original position, as obtained for the pristine electrode. These observations support the inference that the VHCF electrodes, as prepared in this study, are capable of storing ions in their interstitial sites via intercalation, like other PBAs, from a feed solution. The counter-intuitive expansion and contraction of the lattice following its deintercalation and intercalation, respectively, is characteristic of the PBAs and has been reported and explained in literature before.[66,67] For VHCF, the lattice contracts more during insertion of Na^+ in comparison to Ca^{2+}. This would indicate a higher strain for the (de)intercalation of Na^+ than that of Ca^{2+}, making it less attractive for the VHCF electrode. This observation is similar to the higher lattice strain associated with Na^+ (de)intercalation, in comparison to K^+, in a copper hexacyanoferrate (CuHCF) lattice which prefers K^+ over Na^+.[68]

3.3. Selective Ion Separation

The CV and post-mortem XRD analyses, although insightful, only provide an indication of the different affinity of the VHCF electrodes toward mono- and divalent ions. A more direct understanding of the selective ion separation was obtained by treating multivalent ion feeds F1–F3 with a hybrid CDI cell containing VHCF sheet electrodes as a cathode and activated carbon as anode, as shown in Figure 1. The concentrations of the feeds F1–F4 are given in Table 1. The feeds were either binary or ternary mixtures of monovalent alkali metal and divalent alkali earth metal ions. The concentration profiles of the dilute reservoirs containing Li, Na, Ca, and Mg ions are shown in Figure S6 (Supporting Information), and the concentration differences calculated during multiple adsorption steps for each cation are presented in **Figure 4**. It is clear from the four panels that among the ions tested here, VHCF electrodes prefer divalent ions over monovalent ions. This implies that the larger (hydrated) divalent Ca and Mg ions were preferentially absorbed over smaller (hydrated) monovalent Li and Na ions. This preference, or selectivity, can be quantified in terms of a separation factor,[35,41,69] β, calculated as

$$\beta_{1/2} = \left(\frac{c_{1,initial} - c_{1,final}}{c_{2,initial} - c_{2,final}} \right) \left(\frac{c_{2,initial}}{c_{1,initial}} \right) \tag{1}$$
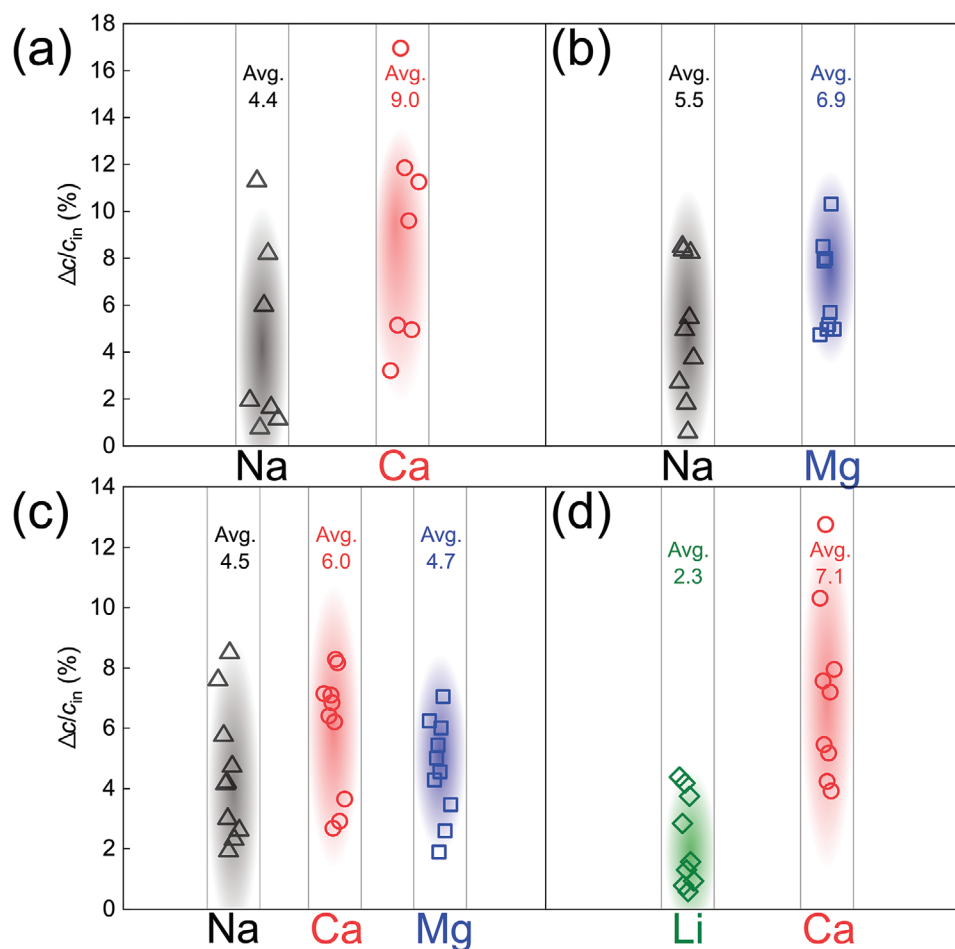

Figure 4. Change in cation concentration in the diluate relative to inlet concentration for feeds a) F1, b) F2, c) F3, and d) F4 after each adsorption cycle. The pH of the feed solutions is given in Table 1.

where 1 is the target ion, 2 is the competitive ion, $c_{1,initial}$, $c_{1,final}$, $c_{2,initial}$, and $c_{2,final}$ are the concentrations of the ions 1 and 2, respectively, in the beginning and at the end of the intercalation step. The data presented in Figure 4a gives a $\beta_{Ca/Na}$ of ≈ 3.5, calculated for each pair of concentration differences and then averaged over the six absorption steps. This manifests as a difference in concentration profiles, as Figure S6a (Supporting Information) shows, where in seven adsorption steps, less than 30% of the starting amount of Na$^+$ was removed while more than 50% of Ca^{2+} was removed, clearly highlighting the preference of the VHCF ions. In Figure 4a, this is corroborated by the higher average Δc values for Ca^{2+} than Na$^+$. The average $\beta_{Ca/Na}$ value obtained here compares remarkably well with CDI selectivity in the range of $2.5 < \beta_{Ca/Na} < 5.5$ was obtained with modified carbon electrodes.[14] In MCDI, where membranes are responsible for the selectivity, the values again ranged between $3 < \beta_{Ca/Na} < 6$.[14] It must be pointed out that the $\beta_{Ca/Na} \approx 6$ was the highest and not the average value, performed with flow electrodes.[70]

The trend was maintained for the feed F2, as the divalent Mg^{2+} was removed more than the monovalent Na ions, as shown from the higher average Δc values for Mg^{2+} than Na$^+$. However, the average $\beta_{Mg/Na}$ of 1.5 is lower than the $\beta_{Ca/Na}$. This may be attributed to the higher dehydration energy of Mg^{2+} (2000 kJ mol^{-1}) than Ca^{2+} (1600 kJ mol^{-1}),[71] which makes the intercalation of Mg^{2+} more difficult than that of Ca^{2+}.

This also becomes clear from Figure 4c where all three ions were present in one mixture. Clearly, divalent ions (Ca and Mg) together were adsorbed more than the monovalent Na$^+$. This contrasts with the affinity demonstrated by NiHCF, which shows high selectivity toward monovalent ions,[35] even though it has similar physical properties as VHCF, as

described in Section 3.1. It is suggested that between the ions of the same valence, the selective separation is based on the dehydration energy of the ions. However, when ions of two different valences are present, the VHCF electrodes prefer divalent over monovalent ions. This is further supported by the result in Figure 4d where a further increase in the dehydration energy of the monovalent ion (from Na$^+$ to Li$^+$) results in its increased rejection, apparent in the higher difference between the Δc values of Li$^+$ and Ca^{2+} and the increased $\beta_{Ca/Li} \approx 4.5$. This becomes more clear in the concentration profile, given in Figure S6d (Supporting Information), where in seven intercalation steps, less than 20% of Li$^+$ was adsorbed while more than 50% of Ca^{2+} was adsorbed by the VHCF electrode.

The DFT calculations paint a similar picture on ion-selectivity with VHCF electrodes to the experiments (**Figure 5**). For comparison, calculations on the intercalation in NiHCF electrodes were also studied. It is clear from Figure 5a that the intercalation of monovalent Na$^+$ into a NiHCF unit cell is thermodynamically more favorable than the divalent Ca^{2+}. The absorption energy for Na$^+$ (ΔE_{Na}) stabilized in the interstitial site of NiHCF was calculated to be -4.17 eV, while it was -3.72 eV for Ca^{2+} (ΔE_{Ca}), indicating a stronger interaction between Na$^+$ and NiHCF and the preference of the NiHCF toward Na$^+$ over Ca^{2+}. This observation is consistent with what has already been reported for experiments in literature about NiHCF electrodes in CDI.[35] In contrast, the intercalation of Ca^{2+} into a VHCF unit cell results in calculated absorption energy of -7.08 eV, indicating a stronger affinity of VHCF toward Ca^{2+} compared to the intercalation of Na$^+$ into the same lattice, of which the absorption energy was found to be -4.02 eV, as shown in Figure 5b. This result shows the opposite preference of the VHCF lattice toward divalent Ca^{2+} in comparison to the NiHCF
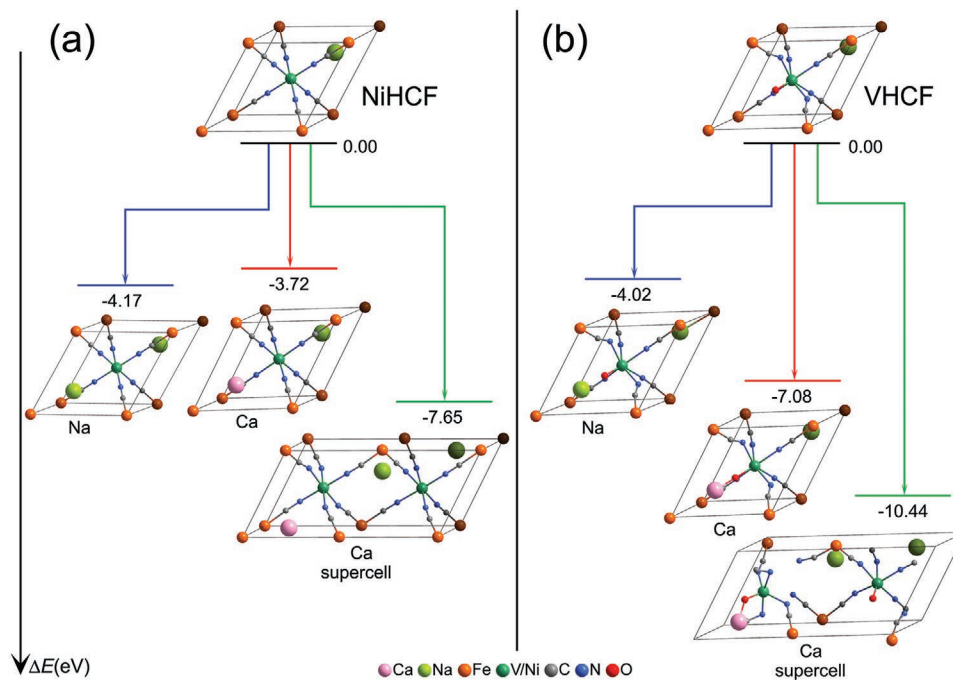

Figure 5. Results of DFT simulations performed to calculate the change in the energy of a unit cell and a $2 \times 1 \times 1$ supercell, that is a combination of two unit cells, of a) NiHCF and b) VHCF following absorption/intercalation of Na$^+$ and Ca^{2+} into the interstitial site.

lattice. Comparison of the absorption energies of Ca^{2+} into the lattices of NiHCF and VHCF reveals that the ΔE_{Ca} is larger for VHCF (−7.08 eV) than that for NiHCF (−3.72 eV). This implies that the Ca^{2+} is accommodated better in VHCF than NiHCF and will, therefore, be more likely to be preferred by the VHCF lattice.

This preference holds for both: a single unit cell where the $(V=O)^{2+}$ and the Fe^{3+} present in the lattice can, upon reduction, accommodate a divalent ion, according to the electrochemical reaction described by the expression of $Ca^{2+} + 2e^- + Na(VO)^{2+}Fe^{3+}(CN)_6 \leftrightarrows CaNa(VO)^+Fe^{2+}(CN)_6$. However, upon reduction, a $2 \times 1 \times 1$ super cell is formed that is a combination of two unit cells. In this super cell structure, an intercalation of a divalent cation requires two Fe^{3+} per cell to be reduced, according to the electrochemical reaction: $Ca^{2+} + 2e^- + (Na(VO)^{2+}Fe^{3+}(CN)_6)_2 \leftrightarrows Ca(Na(VO)^{2+}Fe^{2+}(CN)_6)_2$, as otherwise Ca^{2+} would need to be reduced, which is energetically highly unfavorable. Furthermore, the ΔE_{Ca} for the NiHCF and VHCF supercells were calculated to be −7.65 and −10.44 eV, respectively, making it evident that Ca^{2+} is the preferred cation for intercalation in VHCF over NiHCF. It can be argued, on the basis of similar ΔE_{Na} values for NiHCF and VHCF (−4.17 eV vs −4.02 eV, respectively), that the replacement of Ni with a V=O group has little influence on the intercalation of the monovalent Na^+, but a drastic influence on the intercalation of divalent Ca^{2+}, which is evident from the significant difference between ΔE_{Ca} values for NiHCF and VHCF, as presented in Figure 5a,b (−3.72 eV vs −7.08 eV for a unit cell, and −7.65 eV vs −10.44 eV for a supercell). In view of these predictions, it is proposed that the O atom in the interstitial lattice of VHCF may have a higher coulombic attraction towards the divalent Ca^{2+} than the monovalent Na^+, leading to the switched preference of the VHCF lattice and a larger ΔE_{Ca}. However, this remains a hypothesis, and a further combination of experiments and simulations will be required to elucidate the exact selectivity mechanism in the VHCF lattice. Results from the calculation of the absorption energies of hydrated Na^+ and Ca^{2+} are summarized in the supporting information (Figure S7, Supporting Information). The model again predicted that the intercalation of the hydrated Ca^{2+} in the lattice of VHCF is thermodynamically favorable over that of the hydrated Na^+. However, the hydration model also predicted slightly easier intercalation of Ca^{2+} into the NiHCF lattice, as can be seen by the ΔE_{Ca} and ΔE_{Na} numbers. This discrepancy could be because such simplified hydration models are not accurate enough to describe the solvent structures.[55]

3.4. Electrode Stability

The long-term stability of the electrode was assessed by operating the hybrid CDI cell, containing the VHCF electrode in NaCl and $CaCl_2$ single salt solutions for 40 charge/discharge cycles, in a constant-voltage mode. A sample $CaCl_2$ concentration profile, along with the current, is presented in Figure S8a (Supporting Information), and the post-mortem XRD analysis of the oxidized electrodes, obtained after operation for 40 cycles in NaCl and $CaCl_2$, are provided in **Figure 6**. Nearly all the planes present initially in the pristine electrode were preserved after 40 charge/discharge cycles, demonstrating that the
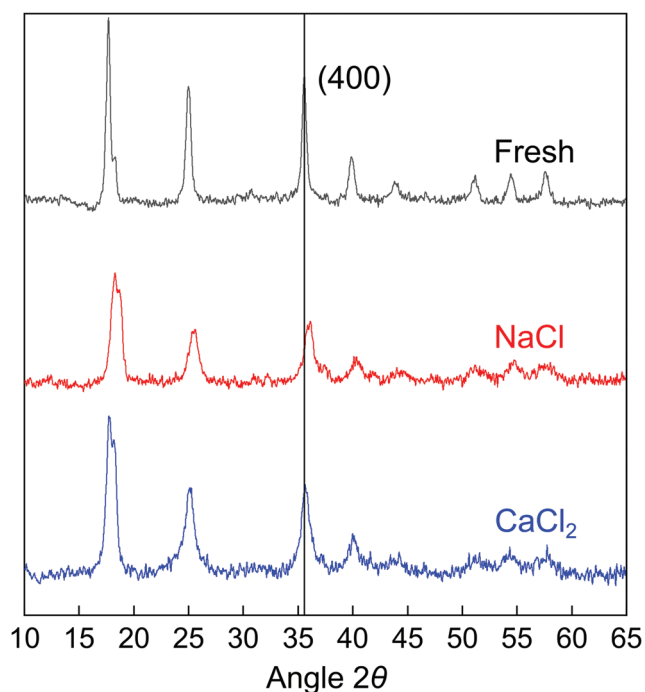

Figure 6. The XRD pattern of the pristine electrode before (black) and after 40 cycles in 20×10^{-3} M single-salt solutions of NaCl (red) and $CaCl_2$ (blue). The (400) peak is marked by a straight vertical line.

structural integrity of the VHCF lattice remained intact after the repeated (de)intercalation of both Na^+ and Ca^{2+}. Furthermore, a comparison of the position of the (400) peak in the X-ray diffractogram of the pristine electrode with that of the electrodes cycled in NaCl, and $CaCl_2$ shows that the lattice contracted after cycling in NaCl, while remaining nearly the same after cycling in $CaCl_2$, indicating the smaller change in the lattice following Ca^{2+} (de)intercalation.

During the long-term cycling experiments with bare VHCF electrodes, it was observed that in the absorption step of the desalination process, a part of the VHCF electrode degraded and dissolved into the treated solution. In more detail, the degradation was observed by the change in the color of the diluate to yellow, indicating that iron hexacyanoferrate had leached into the diluate. It can be attributed to the experimental conditions such as low electrolyte concentration ($\approx20 \times 10^{-3}$ M) and neutral pH implemented in this study, against the high concentrations (1 M) and low pH (<1) as frequently used in literature[32,72] that can affect the stability of the electrodes.[21] This degradation is also reflected in the reduced capacity of the electrode to adsorb Ca^{2+} with the increasing number of cycles, and in the charge efficiency (Λ) values, as shown in Figure S8c (Supporting Information). The Λ values, calculated as the ratio of the ions adsorbed (in coulombs) and the charge input in one half cycle, gradually reduced with time, indicating electrode degradation. In an attempt to prevent the leaching of the electrode into the treated water, an electro-polymerization of PSS-doped PPy conductive polymer, PPy/PSS, was carried out on the surface of the VHCF electrodes, inspired by the use of PPy as a protection against corrosion in metals.[73] A schematic that illustrates the coating, its structure and electrodeposition, is shown
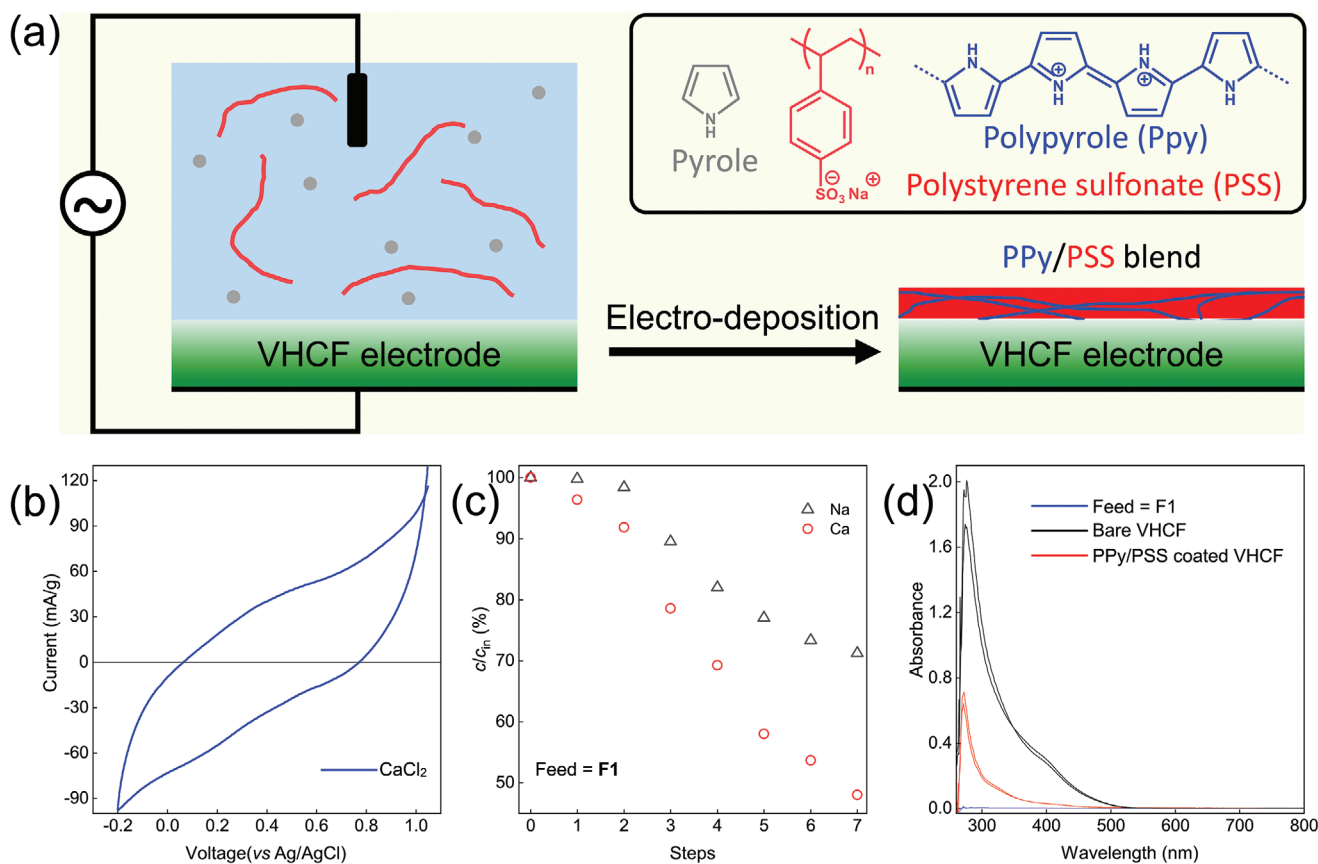
Figure 7. Enhanced stability of the VHCF electrodes by a protective layer of PSS-doped PPy on its surface. a) Schematic of the VHCF electrodeposition with the conductive polymeric coating. b) Cyclic voltammogram of the PPy/PSS-coated VHCF electrode, obtained from CV performed in 1 M CaCl$_2$ electrolyte at a scan rate of 1 mV s^{-1}. c) Concentration of Na$^+$ and Ca^{2+} in the diluate reservoir prior to the treatment of feed F1 by the hybrid cell containing PPy/PSS coated VHCF cathode and an activated carbon anode. d) A UV–vis spectrum of the fresh feed F1 (blue), the diluate treated by hybrid cell containing a bare VHCF electrode (black), and the diluate treated by a hybrid cell containing a PPy/PSS-coated VHCF electrode (red).

in **Figure 7a**. During the oxidation of pyrrole moieties in the polymer formation of PPy, their positive charge is counterbalanced by the negative charge of the PSS. During the reduction of the pyrrole moieties, however, PSS is trapped in between the PPy, and thus, its negative charge will now need to be counterbalanced by the cations present in the solution. So, by doping the PPy with PSS, an anion exchanger was converted into a cation exchanger, matching the property of the VHCF electrodes.

A cyclic voltammogram of VHCF electrode, obtained in a 1 M CaCl$_2$ solution at pH = 7, is provided in Figure 7b. The VHCF electrode remained electrochemically unchanged after the electro-polymerization step, which is evident from the voltammogram (Figure 7b). The conductive polymeric layer did not contribute to any reversible/irreversible reactions during the oxidation as well as the reduction step; the area enclosed by the voltammogram was 40 C g$_{VHCF}^{-1}$, comparable to values obtained for bare VHCF electrodes. A CV, performed in CaCl$_2$ on a graphite paper coated only with the PPy/PSS, shows no reaction peaks during the oxidation and the reduction steps (Figure S9, Supporting Information). This confirms that the PPy/PSS coating did not interfere with the preference of the electrode toward divalent ions, as shown in Figure 7c. When feed F1 was treated with PPy/PSS-coated VHCF, the resulting cation concentrations in the diluate were like those obtained with bare VHCF

electrodes (Figure 4a). The coated VHCF electrodes reduced the Ca^{2+} concentration by more than 50% while removing less than 30% of the Na$^+$ in that same time. A sample concentration and current profile obtained from the desalination of 20 × 10^{-3} M CaCl$_2$ feed with PPy/PSS-coated VHCF electrode is presented in Figure S8b (Supporting Information). The concentration profile shows improvement in calcium absorption, as confirmed by the calcium intake by the cathode, shown in Figure S8c (Supporting Information). However, after 25 cycles, the coated electrodes show a capacity fade. For bare electrodes, this happens after 20 cycles. Figure 7d shows the comparison between the UV–vis spectrum of the fresh feed F1 and the diluate produced after the selectivity experiments performed on feed F1 using the bare VHCF (black curve) and the PPy/PSS coated VHCF electrodes (red curve). As expected, the fresh solution remained free of any iron impurity. The diluate produced after treatment with bare VHCF electrodes gave a strong absorption peak at ≈420 nm, confirming the presence of a [Fe(CN)$_6$]$^{3-}$ group in it.[74] This points to electrode degradation during intercalation. Lattices that lose a [Fe(CN)$_6$]$^{3-}$ unit will not undergo a reduction (intercalation), since the Fe^{3+} atom is removed from it, and as a result, the overall capacity of the electrode will decrease. The electrode degraded foremost in the beginning and then became stable after four cycles, as seen in the UV–vis absorption spectra that

converged at the same concentration level. A further look at the UV–vis absorption spectra reveals that the PPy/PSS layer prevented the leaching of the $[Fe(CN)_6]^{3-}$ and kept its concentration significantly lower in the diluate, when compared with that for the bare VHCF electrode. In addition, no PSS was detected in the diluate. So, while the PPy/PSS was successful in preventing the contamination of the treated stream, its effect on preventing electrode degradation requires further improvement.

Finally, as a check to establish that the PSS ion is held inside the PPy and is not released into the treated solution, a bare piece of graphite (i.e., without the VHCF electrode), electropolymerized with PPy/PSS was analyzed in XPS, after reduction and oxidation steps, as shown in Figure S10 (Supporting Information). The nitrogen/sulfur ratio, representative of the PPy/PSS, was similar for both the oxidized as well as the reduced sample of PPy/PSS coated graphite plate, with a value of ≈1.7 for the oxidized and ≈1.5 for the reduced sample, indicating the stability of the layer. This provides a simple and elegant solution to the issue of feed contamination by electrode degradation.

4. Conclusion

The substitution of nickel with vanadium in the lattice of a PBA switches its preference in CDI experiments from monovalent ions toward divalent ions. This finding provides the first correlation between the substituent transition metal ion in a PBA and the preference of the resulting PBA toward different ions, and opens vast possibilities for tuning PBA selectivity according to the desired application, within the framework of ion-selective CDI. A simple coprecipitation method was used to prepare VHCF with crystals of quality on par with those presented in the literature. In addition, divalent ions were selectively inserted into the VHCF lattice for the first time, proof of which was obtained by cyclic voltammetry, X-ray diffraction, and ion adsorption experiments. Furthermore, intercalation of cations was studied via DFT simulations, and the preliminary results indicated a preference of VHCF toward divalent ions, in contrast to what is usually observed for PBAs, likely resulting from the presence of an adjacent oxygen atom, attached to the vanadium, in the lattice. Finally, a simple solution to prevent leaching of the electrode into the treated water was provided by electro-polymerizing a conducting polymer polypyrrole, doped with PPy/PSS on its surface, essentially cutting off the direct contact with the feed solution. This layer, as shown in this work, does not alter the characteristics of the VHCF electrode in any significant way and effectively prevents the contamination of treated water due to electrode degradation, which has frequently been encountered in CDI with PBAs.

Supporting Information

Supporting Information is available from the Wiley Online Library or from the author.

Acknowledgements

Conflict of Interest

The authors declare no conflict of interest.

Data Availability Statement

Research data are not shared.

Keywords

[1] K. Singh, S. Porada, H. D. de Gier, P. M. Biesheuvel, L. C. P. M. de Smet, *Desalination* **2019**, *455*, 115.
[2] S. Porada, R. Zhao, A. Van Der Wal, V. Presser, P. M. Biesheuvel, *Prog. Mater. Sci.* **2013**, *58*, 1388.
[3] J. Lee, S. Kim, C. Kim, J. Yoon, *Energy Environ. Sci.* **2014**, *7*, 3683.
[4] S. Kim, J. Lee, C. Kim, J. Yoon, *Electrochim. Acta* **2016**, *203*, 265.
[5] S. Porada, L. Weinstein, R. Dash, A. Van Der Wal, M. Bryjak, Y. Gogotsi, P. M. Biesheuvel, *ACS Appl. Mater. Interfaces* **2012**, *4*, 1194.
[6] R. L. Zornitta, K. M. Barcelos, F. G. E. Nogueira, L. A. M. Ruotolo, *Carbon* **2020**, *156*, 346.
[7] Z.-H. Huang, Z. Yang, F. Kang, M. Inagaki, *J. Mater. Chem. A* **2017**, *5*, 470.
[8] E. Frackowiak, F. Béguin, *Carbon* **2001**, *39*, 937.
[9] M. E. Suss, S. Porada, X. Sun, P. M. Biesheuvel, J. Yoon, V. Presser, *Energy Environ. Sci.* **2015**, *8*, 2296.
[10] C. Kim, P. Srimuk, J. Lee, S. Fleischmann, M. Aslan, V. Presser, *Carbon* **2017**, *122*, 329.
[11] A. Omosebi, X. Gao, J. Landon, K. Liu, *ACS Appl. Mater. Interfaces* **2014**, *6*, 12640.
[12] R. L. Zornitta, P. Srimuk, J. Lee, B. Krüner, M. Aslan, L. A. M. Ruotolo, V. Presser, *ChemSusChem* **2018**, *11*, 2101.
[13] M. E. Suss, *J. Electrochem. Soc.* **2017**, *164*, E270.
[14] J. G. Gamaethiralalage, K. Singh, S. Sahin, J. Yoon, M. Elimelech, M. E. Suss, P. Liang, P. M. Biesheuvel, R. L. Zornitta, L. C. P. M. de Smet, *Energy Environ. Sci.* **2021**, *14*, 1095.
[15] P. M. Biesheuvel, A. van der Wal, *J. Membr. Sci.* **2010**, *346*, 256.
[16] R. L. Zornitta, L. A. M. Ruotolo, *Chem. Eng. J.* **2018**, *332*, 33.
[17] J. Lee, P. Srimuk, R. L. Zornitta, M. Aslan, B. L. Mehdi, V. Presser, *ACS Sustainable Chem. Eng.* **2019**, *7*, 10132.
[18] J. Lee, S. Kim, J. Yoon, *ACS Omega* **2017**, *2*, 1653.
[19] S. Porada, A. Shrivastava, P. Bukowska, P. M. Biesheuvel, K. C. Smith, *Electrochim. Acta* **2017**, *255*, 369.

**ADVANCED
SCIENCE NEWS**

www.advancedsciencenews.com

**ADVANCED
FUNCTIONAL
MATERIALS**

www.afm-journal.de

[20] R. Y. Wang, B. Shyam, K. H. Stone, J. N. Weker, M. Pasta, H. W. Lee, M. F. Toney, Y. Cui, *Adv. Energy Mater.* **2015**, *5*, 1.

[21] P. Marzak, J. Yun, A. Dorsel, A. Kriele, R. Gilles, O. Schneider, A. S. Bandarenka, *J. Phys. Chem. C* **2018**, *122*, 8760.

[22] B. W. Byles, B. Hayes-Oberst, E. Pomerantseva, *ACS Appl. Mater. Interfaces* **2018**, *10*, 32313.

[23] P. Srimuk, F. Kaasik, B. Kruner, A. Tolosa, S. Fleischmann, N. Jackel, M. C. Tekeli, M. Aslan, M. E. Suss, V. Presser, *J. Mater. Chem. A* **2016**, *4*, 18265.

[24] Y. Liu, Y. Qiao, W. Zhang, Z. Li, X. Ji, L. Miao, L. Yuan, X. Hu, Y. Huang, *Nano Energy* **2015**, *12*, 386.

[25] R. Wang, S. Lin, *J. Colloid Interface Sci.* **2020**, *574*, 152.

[26] K. Singh, L. Zhang, H. Zuilhof, L. C. P. M. de Smet, *Desalination* **2020**, *496*, 114647.

[27] S. Kim, H. Yoon, D. Shin, J. Lee, J. Yoon, *J. Colloid Interface Sci.* **2017**, *506*, 644.

[28] P. Srimuk, J. Lee, S. Fleischmann, M. Aslan, C. Kim, V. Presser, *ChemSusChem* **2018**, *11*, 2091.

[29] A. A. Karyakin, *Electroanalysis* **2001**, *13*, 813.

[30] C. D. Wessells, S. V. Peddada, R. A. Huggins, Y. Cui, *Nano Lett.* **2011**, *11*, 5421.

[31] S. Choi, B. Chang, S. Kim, J. Lee, J. Yoon, J. W. Choi, *Adv. Funct. Mater.* **2018**, *28*, 1802665.

[32] J. H. Lee, G. Ali, D. H. Kim, K. Y. Chung, *Adv. Energy Mater.* **2017**, *7*, 1601491.

[33] M. Jayalakshmi, F. Scholz, *J. Power Sources* **2000**, *91*, 217.

[34] Y. Moritomo, S. Urase, T. Shibata, *Electrochim. Acta* **2016**, *210*, 963.

[35] K. Singh, Z. Qian, P. M. Biesheuvel, H. Zuilhof, S. Porada, L. C. P. M. de Smet, *Desalination* **2020**, *481*, 114346.

[36] T. Kim, C. A. Gorski, B. E. Logan, *Environ. Sci. Technol. Lett.* **2017**, *4*, 444.

[37] V. Pothanamkandathil, J. Fortunato, C. A. Gorski, *Environ. Sci. Technol.* **2020**, *54*, 3653.

[38] V. D. Neff, *J. Electrochem. Soc.* **1978**, *125*, 886.

[39] L. F. Schneemeyer, S. E. Spengler, D. W. Murphy, *Inorg. Chem.* **1985**, *24*, 3044.

[40] T. Ikeshoji, *J. Electrochem. Soc.* **1986**, *133*, 2108.

[41] T. Kim, C. A. Gorski, B. E. Logan, *Environ. Sci. Technol. Lett.* **2018**, *5*, 578.

[42] K. Singh, S. Sahin, J. G. Gamaethiralalage, R. L. Zornitta, L. C. P. M. de Smet, *Chem. Eng. J.* **2021**, 128329.

[43] C. D. Wessells, S. V. Peddada, M. T. McDowell, R. A. Huggins, Y. Cui, *J. Electrochem. Soc.* **2012**, *159*, A98.

[44] J. Lee, P. Srimuk, K. Aristizabal, C. Kim, S. Choudhury, Y.-C. Nah, F. Mücklich, V. Presser, *ChemSusChem* **2017**, *10*, 3611.

[45] G. Kresse, J. Furthmüller, *Phys. Rev. B: Condens. Matter Mater. Phys.* **1996**, *54*, 11169.

[46] S. Porada, P. Bukowska, A. Shrivastava, P. M. Biesheuvel, K. C. Smith, *arXiv Prepr. arXiv1612.08293* **2016**, *255*, 1.

[47] M. Aslan, M. Zeiger, N. Jäckel, I. Grobelsek, D. Weingarth, V. Presser, *J. Phys. Condens. Matter* **2016**, *28*, 114003.

[48] X. Gao, S. Porada, A. Omosebi, K. L. Liu, P. M. Biesheuvel, J. Landon, *Water Res.* **2016**, *92*, 275.

[49] G. Kresse, D. Joubert, *Phys. Rev. B* **1999**, *59*, 1758.

[50] J. P. Perdew, K. Burke, M. Ernzerhof, *Phys. Rev. Lett.* **1996**, *77*, 3865.

[51] P. E. Blöchl, *Phys. Rev. B* **1994**, *50*, 17953.

[52] A. Shrivastava, S. Liu, K. C. Smith, *Phys. Chem. Chem. Phys.* **2019**, *21*, 20177.

[53] B. Stahl, T. Bredow, *J. Comput. Chem.* **2020**, *41*, 258.

[54] S. Grimme, S. Ehrlich, L. Goerigk, *J. Comput. Chem.* **2011**, *32*, 1456.

[55] Y. Xu, H. Zhou, G. Wang, Y. Zhang, H. Zhang, H. Zhao, *ACS Appl. Mater. Interfaces* **2020**, *12*, 41437.

[56] M. A. Lumley, D. H. Nam, K. S. Choi, *ACS Appl. Mater. Interfaces* **2020**, *12*, 36014.

[57] S. Kjeldgaard, I. Dugulan, A. Mamakhel, M. Wagemaker, B. B. Iversen, A. Bentien, *R. Soc. Open Sci.* **2021**, *8*, 201779.

[58] M. K. Carpenter, R. S. Conell, S. J. Simko, *Inorg. Chem.* **1990**, *29*, 845.

[59] C. G. Tsiafoulis, P. N. Trikalitis, M. I. Prodromidis, *Electrochem. Commun.* **2005**, *7*, 1398.

[60] N. Imanishi, T. Morikawa, J. Kondo, R. Yamane, Y. Takeda, O. Yamamoto, H. Sakaebe, M. Tabuchi, *J. Power Sources* **1999**, *81*, 530.

[61] X. Sun, V. Duffort, L. F. Nazar, *Adv. Sci.* **2016**, *3*, 1600044.

[62] F. A. Miller, C. H. Wilkins, *Anal. Chem.* **1952**, *24*, 1253.

[63] S. N. Ghosh, *J. Inorg. Nucl. Chem.* **1974**, *36*, 2465.

[64] Y. Xu, M. Chang, C. Fang, Y. Liu, Y. Qiu, M. Ou, J. Peng, P. Wei, Z. Deng, S. Sun, X. Sun, Q. Li, J. Han, Y. Huang, *ACS Appl. Mater. Interfaces* **2019**, *11*, 29985.

[65] X. Peng, H. Guo, W. Ren, Z. Su, C. Zhao, *Chem. Commun.* **2020**, *56*, 11803.

[66] K. Hurlbutt, S. Wheeler, I. Capone, M. Pasta, *Joule* **2018**, *2*, 1950.

[67] C. D. Wessells, R. A. Huggins, Y. Cui, *Nat. Commun.* **2011**, *2*, 2.

[68] P. Jiang, H. Shao, L. Chen, J. Feng, Z. Liu, *J. Mater. Chem. A* **2017**, *5*, 16740.

[69] S. D. Rassat, J. H. Sukamto, R. J. Orth, M. A. Lilga, R. T. Hallen, *Sep. Purif. Technol.* **1999**, *15*, 207.

[70] C. He, J. Ma, C. Zhang, J. Song, T. D. Waite, *Environ. Sci. Technol.* **2018**, *52*, 9350.

[71] Y. Marcus, *Biophys. Chem.* **1994**, *51*, 111.

[72] B. Paulitsch, J. Yun, A. S. Bandarenka, *ACS Appl. Mater. Interfaces* **2017**, *9*, 8107.

[73] M. I. Redondo, C. B. Breslin, *Corros. Sci.* **2007**, *49*, 1765.

[74] C. R. Susana, P. J. Jorge, H. Pablo, M. L. M. Luis, M. Paul, *Langmuir* **2010**, *26*, 1271.